JOURNAL OF GEOPHYSICAL RESEARCH, VOL. 104, NO. D18, PAGES 22,301–22,318, SEPTEMBER 27, 1999

A ray-tracing operator and its adjoint for the use of GPS/MET refraction angle measurements

X. Zou,[1] F. Vandenberghe,[2] B. Wang,[1,3] M. E. Gorbunov,[4] Y.-H. Kuo,[2] S. Sokolovskiy,[4] J. C. Chang,[5] J. G. Sela,[6] and R. A. Anthes[7]

Abstract. The development of small, high-performance instruments to receive Global Positioning System (GPS) signals has created an opportunity for active remote sounding of the Earth's atmosphere by radio occultation techniques. A prototype demonstration of this capability has been provided by the GPS Meteorology (GPS/MET) experiment. Although it was shown that high vertical resolution profiles of atmospheric refractivity, temperature, and geopotential height of constant pressure levels can be derived from the GPS measurements, with high accuracy under many circumstances, many issues remain. These include the existence of multipath propagation, the ambiguity between water vapor and temperature in moist regions of the atmosphere, and the difficulty in retrieving an accurate refractivity profile from the GPS refraction angle measurements over regions where the horizontal gradient of the refractivity is large. The aim of this paper is to begin the development of a methodology for incorporating the GPS "raw" measurements (refraction angles) directly into numerical weather analysis and/or prediction systems in order to alleviate the above mentioned problems. First, a ray-tracing observation operator that links the atmospheric state to the GPS refraction angle measurements is developed, the physics and numerics involved are described, and the simulated refraction angles, based on the NOAA National Centers for Environmental Prediction (NCEP) global analysis, are compared with the observed GPS/MET refraction angle measurements. Second, the tangent linear and adjoint of the ray-tracing operator are developed. These three operators are required for the direct use of GPS refraction angle measurements in a variational data analysis system. A single observation experiment reveals that the direct use of GPS refraction angles in a variational analysis causes changes in the temperature and specific humidity fields that are not limited to the occultation location but in an elongated band of ± 300 km in its occultation plane. On σ-levels, changes from the use of one GPS occultation occur in an area of about 600 km $\times$ 600 km large which is centered around the ray perigee point. Finally, the advantages and disadvantages are discussed for the use of the GPS refractivities versus refraction angles. Errors made by using local estimates of refractivity are also assessed.

1. Introduction

With the advent of the Global Positioning System (GPS) using high-performance transmitters in high orbits and low Earth-orbiting (LEO) satellites equipped with GPS receivers, it is now possible to remotely sound the Earth's atmosphere using radio occultation techniques [*Kursinski et al*., 1997; *Rocken et al*., 1997]. The radio occultation technique has several attractive features: (1) it is not affected by clouds or precipitation; (2) it provides accurate data at high vertical resolution; (3) it does not require any instrument calibration; and (4) its errors are statistically independent of the other types of measurements.

In April 1995 the first GPS/MET instrument package (receiver), placed on a small LEO satellite named MicroLab 1, was launched to collect GPS occultation observations. This proof-of-concept GPS/MET experiment was designed to demonstrate the feasibility of observing the atmosphere by the GPS limb sounding method [*Fjeldbo et al*., 1971]. Approximately 70,000 GPS/MET soundings have been obtained since the initial launch. Many studies have compared the GPS/MET-retrieved temperature profiles with other types of data, such as operational global analysis, radiosondes, and other satellite data [*Ware et al*., 1996; *Kursinski et al*., 1996, 1997; *Rocken et al*., 1997; *Kuo et al*., 1998]. Another study examined the accuracy of GPS/MET-derived geopotential height [*Leroy*, 1997]. All of these studies suggest that GPS/MET occultation measurements have the potential to make a positive impact in numerical weather prediction and climate studies.

The GPS consists of 24 satellites, distributed in six orbit planes about the globe. Each GPS satellite orbit is circular, with an altitude of 20,200 km. The LEO satellite orbit in the GPS/MET experiment is about 730 km. GPS satellites are

[1]Department of Meteorology, Florida State University, Tallahassee.
[2]National Center for Atmospheric Research, Boulder, Colorado.
[3]Institute of Atmospheric Physics, LASG, Chinese Academy of Sciences, Beijing.
[4]Institute of Atmospheric Physics, Moscow, Russia.
[5]Central Weather Bureau, Taipei.
[6]National Centers for Environmental Prediction, Camp Springs, Maryland.
[7]University Corporation for Atmospheric Research, Boulder, Colorado.

Paper number 1999JD900450.
0148-0227/99/1999JD900450$09.00

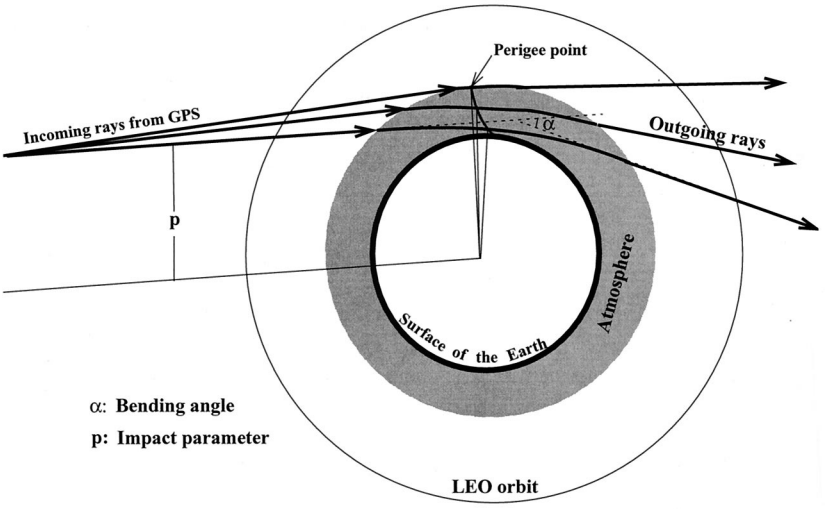

Figure 1. Schematic representation of the bending ray paths.

equipped with transmitters with an extremely high stability of frequency ($\delta f/f \leq 10^{-14}$, where f is the frequency). The GPS receiver, located on an LEO satellite, is capable of tracking the frequency of the received signal with very high accuracy. During an occultation, the satellites move in such a way that the electromagnetic ray connecting them traverses the atmosphere. Because of bending of the ray, by the atmospheric refractivity gradients, the phase of the ray changes. The change of phase in time is tracked by the GPS receiver. The difference between the accumulated phase delay between the two satellites and the phase delay in the vacuum is termed the phase excess.

For a given observation geometry specified by the satellite positions and velocities, the derivative of the phase excess (the Doppler shift excess) characterizes the atmospheric and ionospheric effect on the Doppler frequency shift and can be treated as the basic measurement data. The observed refraction angle α, the angle between the ray tangent vectors at GPS and LEO satellites (see Figure 1), is then derived from the Doppler shift excess with the assumption of the spherical symmetry of refractive index in the atmosphere: $n(\vec{r}) = n(r)$, where $\vec{r}$ is a radius vector and $r = |\vec{r}|$ is the distance of a point on the ray to the Earth's center. Under this assumption the impact parameter, the shortest distance from the ray to the Earth's center multiplied by the refractivity, is constant for a given ray; that is, p is an invariant of the ray trajectory equations:

$$p = n(r)\|(\vec{r} \times \vec{u}^t)\| = \text{ const}, \tag{1}$$

where $\vec{u}^t$ is the unit vector of the tangent direction of the ray. Equation (1), called Snell's law, allows a unique determination of both impact parameter (p) and refraction angle (α) from the Doppler frequency shift (see Appendix, section A1).

When the variation of the refractivity is dominated by the vertical gradient of density, the refraction angle profile, as a function of the impact parameter, can be inverted to obtain the refractivity profile using the Abel transform under the spherical symmetry assumption [*Fjeldbo et al.*, 1971]. One can derive the index of refractivity profile from the following relation:

$$n(a) = \exp\left[\frac{1}{\pi}\int_a^\infty \frac{\alpha(p)}{\sqrt{p^2 - a^2}}\,dp\right], \tag{2}$$

where $a = nr$, r is the distance from the center of curvature. Given $\alpha(p)$, (2) can be evaluated numerically. Atmospheric refractivity N is related to the index of refractivity n through $N = 10^6(n - 1)$. We will denote such derived (and approximate) refractivity from GPS/MET observations as N^{obs} and that from model atmosphere to refraction angle (through ray tracing) and then to refractivity through Abel inversion as N^{GPS}. Both N^{obs} and N^{GPS} are complicated nonlinear functionals of the refractivity on the occultation plane, i.e., the plane defined by GPS, LEO satellite, and the center of curvature of the local atmosphere in the vicinity of the ray perigee. Under the spherical symmetry assumption, the center of curvature of the local atmosphere coincides with the Earth's center.

We indicate that the spherical symmetry assumption is used twice in deriving GPS measurements. It is used first to determine the refraction angle (α) and impact parameter (p) from the frequency data, as well as transmitter and receiver positions, and then to determine the GPS refractivity (N^{obs}) from the dependence of the refraction angle with respect to the impact parameter $\alpha(p)$. Departures from spherical symmetry of the horizontal structure of the atmosphere can lead to serious errors in the resulting GPS measurements of $\alpha(p)$ and N^{obs}. In tropical and other lower-troposphere regions where the humidity has a complicated horizontal structure, more than one ray may arrive at the receiver, a condition known as multipath. Under conditions of multipath, the retrieved refractivity profile may contain significant errors [*Gorbunov and Gurvich*, 1998]. A general quantitative assessment of the errors resulting from unmodeled large-scale horizontal gradients in the atmosphere is currently unavailable.

The atmospheric refractivity depends on the pressure (P), the temperature (T), and the specific humidity (q) in the neutral atmosphere and on the electron density in the ionosphere. Use of two frequencies allows one to eliminate or to considerably remove the ionospheric effects on the refraction angles (although the small-scale ionospheric irregularities may still result in some residual errors, but this effect is not significant at heights below 35 km).

Even with perfect profiles of atmospheric refractivity, calculation of the meteorological values (T, q, and P) directly from the refractivity is an underspecified problem. A refractivity

profile and the hydrostatic equation uniquely define pressure and temperature for the dry atmosphere only. When water vapor contributions to the refractivity are significant, there are two equations (hydrostatic equilibrium and refractivity) and three unknowns (pressure, temperature, and humidity). Independent knowledge of one of the three quantities, pressure, temperature, or humidity, is required in order to calculate the other two [*Ware et al*., 1996].

Emphasis in this paper is placed on developing the concepts underlying a long-term GPS/MET data analysis/assimilation strategy. We propose to incorporate GPS/MET refraction angles (α), as a function of the impact parameter (p), directly into a variational analysis or assimilation system using adjoint techniques. The paper is arranged as follows: In section 2 we describe an observation "ray-tracing" operator for the data analysis using GPS/MET refraction angle measurements. Section 3 presents a series of numerical simulations of GPS/MET refraction angles using the NCEP analysis as input model state for the raytracing operator. Simulated refraction angle profiles based on the National Centers for Environmental Prediction (NCEP) analyses at 1200, 1100, and 0000 UTC, October 12, 1995, are compared with a total of 62 real GPS/MET refraction angle measurements received within this 12-hour time period. In section 4 the development of the tangent linear and adjoint of the ray-tracing operator is described, followed by a single refraction angle observation experiment to examine the distribution of changes in temperature, specific humidity, and refractivity associated with the analysis of a single observation both in the occultation plane and on the model σ levels. Comparisons between the local (true) atmospheric refractivity profiles (N) from the analyses and the simulated GPS-retrieved refractivities (N^{GPS}) are made in section 5. The paper is concluded in section 6.

2. GPS Observation Operator, a Ray-Tracing Algorithm

Direct incorporation of any kind of measurement data requires an observation operator, i.e., an operator mapping the model state vector to the corresponding measurement vector.

The observation operator developed here for the GPS/MET occultation measurements involves a ray-tracing procedure, as well as routines for calculation and interpolation of the refractivity and its gradient onto any arbitrarily chosen point along the rays from gridded model fields of pressure, temperature, and humidity. It uses the traditional ray impact parameter, the perigee point position (the point on the ray which is nearest to the center of the Earth) and orientation of the occultation plane, which can be found from the satellite positions.

Specifically, the GPS observation operator starts with a numerical integration of the ray trajectory equation which, when expressed in a system of Cartesian coordinates, is [*Kravtsov and Orlov*, 1990]

$$\frac{d^2\vec{x}}{d\tau^2} = n\nabla n, \tag{3}$$

where $\vec{x} = (x_1, x_2, x_3)$ is the Cartesian coordinate vector, $\vec{x} = \vec{x}(\tau)$ is the ray trajectory parameterized with a parameter τ, $d\tau = (ds/n)$, s is the length of the ray, and n is the atmospheric index of refractivity.

Equation (3) can be solved numerically for any given field of refractivity index $n(x)$ and initial conditions (position and direction) or boundary conditions (the two given points the ray connects) of the ray. The boundary problem of finding a ray can be solved using a shooting method [*Gorbunov and Sokolovskiy*, 1993]. It might seem to be more appropriate than the initial value problem for modeling GPS measurements, for which we know satellite positions and the phase excess at every moment of time. However, in multipath areas the boundary problem may have multiple solutions that correspond to multipath propagations. This results in the necessity of first determining the total number of rays, which is not known, and then locating these rays. Therefore the basic procedure we are proposing for the ray-tracing operator consists of the solution of the ray problem with given initial conditions. In this case we first compute a range of rays at different perigee heights, then seek the dependence of the refraction angle on the impact parameter, and finally, interpolate this dependence to the same grid as that of the measured dependence. Such a ray-tracing procedure is detailed as follows:

The second-order equation (3) can be rewritten as two coupled first-order equations:

$$\frac{d\vec{x}}{d\tau} = \vec{y}(\tau),$$

$$\frac{d\vec{y}}{d\tau} = n\nabla n, \tag{4}$$

where $\vec{y} = d\vec{x}/d\tau$. The boundary conditions to solve (4) numerically are given by the values of $\vec{x}$ and $\vec{y}$ at a starting point. These values are described as follows:

We use the perigee point location $\vec{x}_p$ and the unit vector $\vec{u}_p^n$ normal to the occultation plane at the perigee point to calculate the tangent vector

$$\vec{u}_p^t = \frac{\vec{x}_p}{|\vec{x}_p|} \times \vec{u}_p^n, \tag{5}$$

where $\vec{u}_p^t$ is the unit vector tangent to the ray at the perigee point. Then a virtual GPS satellite position $\vec{x}_s$ is defined from the perigee point in the opposite direction of the tangent vector at a distance of 20,200 km:

$$\vec{x}_0 = \vec{x}_p - \lambda\vec{u}_p^t, \tag{6}$$

where λ is a constant whose value is found by solving the equation of $\|\vec{x}_0\| = 20{,}200$ km. The values of $\vec{x}_0$ and $\vec{u}_p^t$ ($\vec{u}_p^t$ is used as $\vec{u}_0^t$, the tangent direction of the ray at the initial point) defined in (5) and (6) are used as the initial conditions for $\vec{x}$ and $\vec{y}$ for the ray tracing. The ray equation (4) is solved by either the fourth-order Runge-Kutta method [*Gorbunov et al*., 1996] or the alternating direction implicit (ADI) method. The ADI method is a second-order scheme which conserves the important geometrical structure of the original differential system [*Peaceman and Rachford*, 1955; *Yanenko*, 1971]. The Runge-Kutta method is a classic fourth-order dissipation scheme [*Press et al*., 1992], which will lose the energy of the system during the long-term integration. Using the ADI method, for example, the ray trajectory equation becomes

$$\vec{x}_{m+1} = \vec{x}_m + \Delta\tau\vec{y}_{m+1/2} + \mathrm{O}((\Delta\tau)^3),$$

$$\vec{y}_{m+3/2} = \vec{y}_{m+1/2} + \Delta\tau\vec{f}(\vec{x}_{m+1}) + \mathrm{O}((\Delta\tau)^3), \tag{7}$$

where $m(= 0, 1, \ldots)$ is the index of integration step, $\Delta\tau$ is the interval of the grids on the rays ($\Delta\tau = 30$ km is used in the current model), and

$$\vec{f} = n\nabla n. \tag{8}$$

The ADI method needs an additional initial condition $\vec{y}_{1/2}$, which can be calculated by using the second-order implicit scheme:

$$\vec{y}_{1/2} = \vec{y}_0 + \frac{1}{2}\Delta\tau\vec{f}\left(\vec{x}_0 + \frac{1}{8}\Delta\tau(\vec{y}_{1/2} + \vec{y}_0)\right) + O((\Delta\tau)^3). \tag{9}$$

Examining the numerical procedure of solving the ray equations (7)–(9), we find that values of the model atmospheric refractivity index n and its gradient ∇n on the ray trajectories are required. To calculate refractivity index n and its gradient ∇n in given Cartesian coordinates, we need first to convert the Cartesian coordinates (x_1, x_2, x_3) to geodetic altitude, latitude, and longitude (z, ϕ, λ) (see the Appendix, section A2) and then to interpolate the refractivity from model grids to geodetic altitude, latitude, and longitude grids (see Appendix, section A3).

Numerical integration of the ray equation (7) continues until the rays go out of the atmosphere (the distance from the ray to the Earth's surface $\geq$100 km).

When the ray integration is finished, we obtain the ray position $(\vec{x}_f)$ and the tangent direction $(\vec{u}_f^t)$ at the final point (reception point or LEO position). Then the refraction angle for given impact parameter p at the perigee point location is computed by the angle between the two tangent vectors $\vec{u}_0^t$ and $\vec{u}_f^t$; that is,

$$\alpha(p) = \widehat{(\vec{u}_0^t, \vec{u}_f^t)}, \tag{10}$$

where the hat $(\widehat{\ })$ represents the angle between the two vectors.

The values of the refraction angle α in (10) as a function of the impact parameter p calculated on the basis of the model atmosphere will then be compared with the GPS observed refraction angles α^{obs}. We mention here that the derivation of $\alpha(p)$ using (10) is different from what is described in the Appendix, section A1, for GPS refraction angle measurements. The observed refraction angle is derived under the assumption of the spherical symmetry of refractivity in the atmosphere. If the atmosphere is not spherically symmetric (which is the general case), then we cannot define a single impact parameter for the ray, because p is different at both LEO and GPS locations. The Doppler shift is now a function of $p|_{\text{GPS}}$ and $p|_{\text{LEO}}$, and one number (Doppler shift) does not suffice to calculate two unknowns ($p|_{\text{GPS}}$ and $p|_{\text{LEO}}$). However, we can formally use the same procedure for the impact parameter for the ray as in a spherically symmetric atmosphere. Then both the impact parameter and the refraction angle derived from GPS observational data are not true ones (we cannot define a single impact parameter, and we have insufficient data to calculate the refraction angle in a horizontally inhomogeneous media). Thus we have to consider $\alpha(p)$ as a complicated function of the refractivity field. To be consistent, we must also model the procedure for calculation of $\alpha(p)$ in our observation operator in the same way. However, the difference between $p|_{\text{GPS}}$ and $p|_{\text{LEO}}$ is only significant in the atmospheric boundary layer where $n(\vec{x})$ has strong horizontal gradients. Since we currently have only a few GPS/MET observations in the boundary layer, (10) can be treated as a very good approximation for what we derive from the GPS/MET observational data. In the future, when the quality of the GPS/MET observations in the lower troposphere is improved [*Rocken et al*., 1997], it will be possible to incorporate the calculation of refraction angle through Doppler shift into the observational operator.

An important fact for incorporating the GPS measurements into a variational data analysis system is that the observational data are integral functionals of the atmospheric refractivity and its gradient along the ray. The observations can thus be thought of as a functional specified on the manifold of rays transilluminating the atmosphere. The GPS observation operator developed in this research is based on a ray-tracing algorithm. The corresponding tangent linear model involves the calculation of the response of the ray path to the small variations in the atmospheric state along the ray path.

In the following, we will use **H** to represent all the operations in the ray tracing to obtain a vertical profile $\vec{\alpha}$ of refraction angle from the input of temperature, specific humidity, and surface pressure fields on the NCEP model grids (represented by a vector **x**); that is,

$$\vec{\alpha} = \mathbf{H}(\mathbf{x}), \tag{11}$$

where **x** represents the NCEP model variables of the temperature T and specific humidity q at 28 vertical levels and the surface pressure p_s on all the Gaussian grids.

Differences between the refraction angle profiles derived from the Runge-Kutta method and the ADI method, based on the same analysis, are negligible (figure omitted). However, the CPU time spent in the forward ray-tracing model using the Runge-Kutta method to simulate one GPS occultation (for about 300 rays with 100 integration steps on each ray) is 5.92 s on a Cray C90 machine at NCEP. The CPU time using the ADI method is reduced to 3.25 s. The saving of CPU time for the corresponding tangent linear and adjoint operators, which will be presented in section 4 of this paper, is even greater.

3. Numerical Simulation of GPS/MET Refraction Angles

Most of the published GPS/MET comparison studies were carried out on the basis of retrieved GPS products (e.g., temperature, pressure, geopotential heights). Here we will present some results from a comparison made between refraction angle profiles (derived from NCEP analyses) and actual GPS data, in order to examine how the GPS refraction angle measurements differ from the simulated refraction angles.

We select a 12-hour time period from 1200 UTC, October 11, to 0000 UTC, October 12, 1995, for such a study. Comparison is made with all the actual refraction angle measurements over the whole globe during this time period. While we examine the performance of the forward ray-tracing model, we will summarize some of the characteristics of the differences between the simulated and the observed refraction angles.

Over the entire globe, there are a total of 62 GPS occultations available from the UCAR Payload Operations Control Center (POCC) during the period from 1200 UTC, October 11, to 0000 UTC, October 12, 1995 (Figure 2). This number of observations is much smaller than the theoretical estimate (250 soundings per 12 hours for one GPS receiver) and is caused by a number of factors related to the low budget "piggy back" nature of this proof-of-concept experiment (e.g., only setting occultations were observed and there were limitations in the ground fiducial network).

The GPS occultations in Figure 2 are numbered in the order of their receiving time; that is, the first occultation received

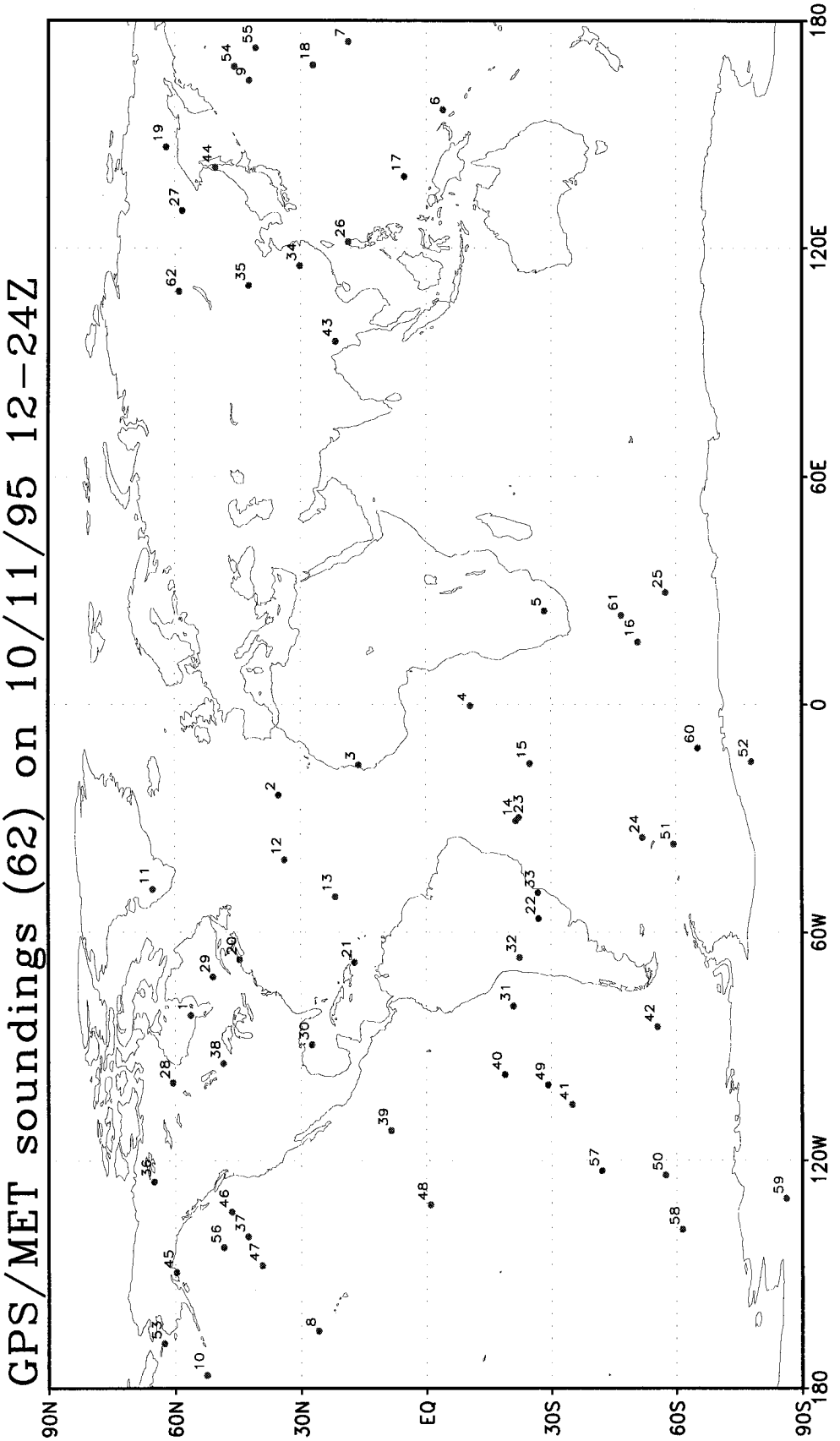

Figure 2. Global coverage of all the GPS occultations received from the MicroLab-1 satellite during a 12-hour period from 1200 UTC, October 11, to 0000 UTC, October 12, 1995. Each occultation is numbered in the order of its receiving time.

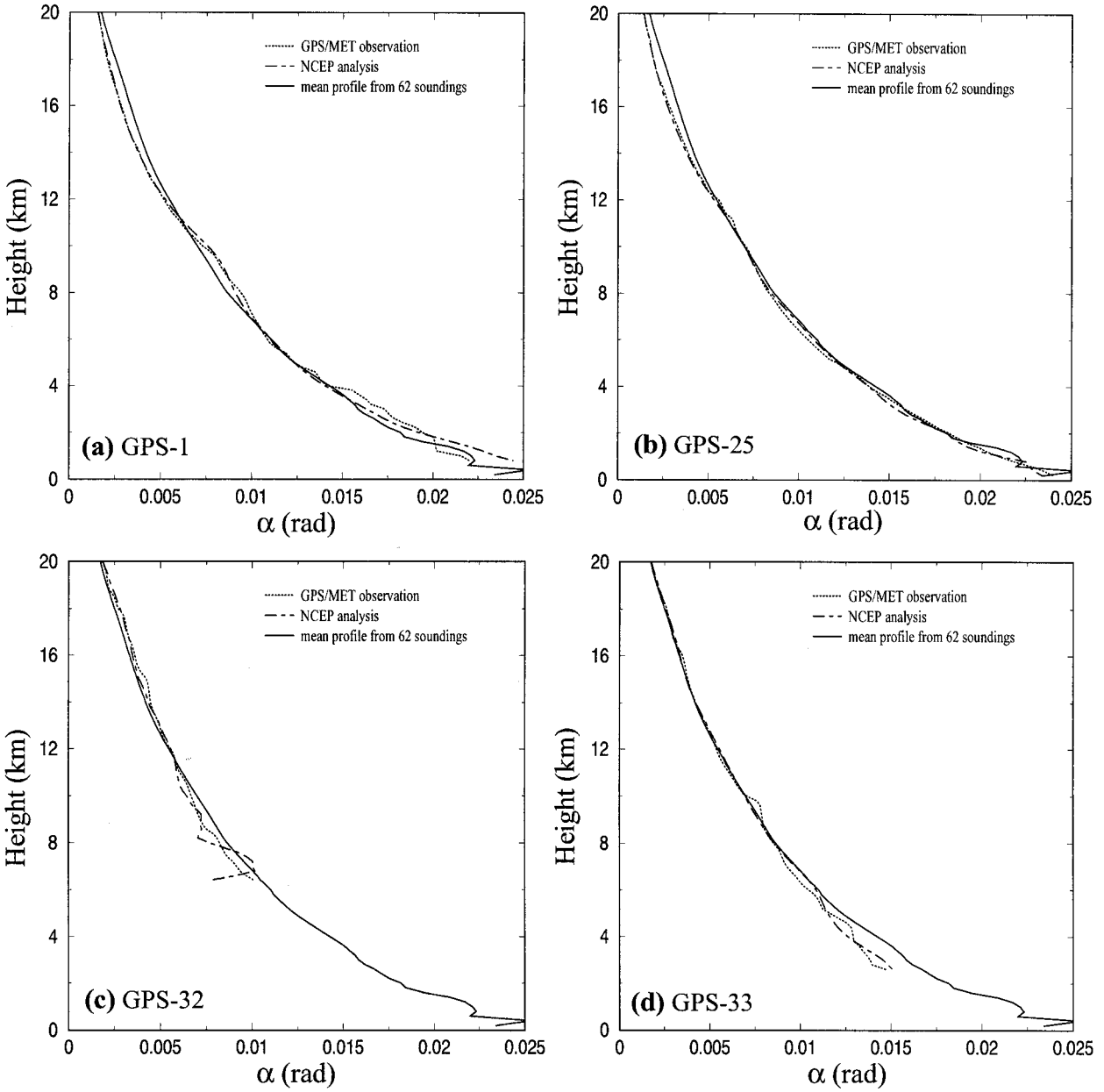

Figure 3. Vertical profiles of refraction angle. (a) GPS-1, (b) GPS-25, (c) GPS-32, and (d) GPS-33. Solid line represents the mean profile (refraction angles averaged over the 62 soundings observed between 1200 UTC, October 11, and 0000 UTC, October 12, 1995; dashed-dotted line represents individual soundings derived from the forward ray-tracing algorithm based on NCEP analysis, and dotted line is the observed GPS refraction angle profiles.

right after 1200 UTC, October 11, is GPS occultation 1 (we will denote it as GPS-1), and the last occultation received during this period is GPS occultation 62 (GPS-62). The first 33 occultations are received before 1800 UTC, October 11, and the rest of the occultations are received after 1800 UTC, October 11.

Examples in Figure 3 show how refraction angle profiles derived from the NCEP analysis using the ray-tracing operator differ from the observed refraction angle profiles. We selected four occultations: GPS-1 and GPS-25 (Figures 3a and 3b) are the two occultations among the 62 occultations that reach the lowest elevations (0.2 km for GPS-1 and 0.8 km for GPS-25); GPS-32 (Figure 3c) is a sounding which we find contains the largest difference between simulated and observed refraction angles in the troposphere between 6 and 8 km; and GPS-33 (Figure 3d) represents a typical sounding. We find that in general, the simulated refraction angles agree very well with the GPS/MET observed ones. Differences between the simulated and the observed refraction angles appear in the troposphere at certain altitudes, which indicates that the GPS/MET observations may contain useful information about the atmospheric state at these heights.

To assess how different the simulated refraction angles are from the observed ones, we study some statistical characteristics of the following error vectors:

$$\Delta\vec{\alpha}_l = \vec{\alpha}_l - \vec{\alpha}_l^{\text{obs}}, \tag{12}$$

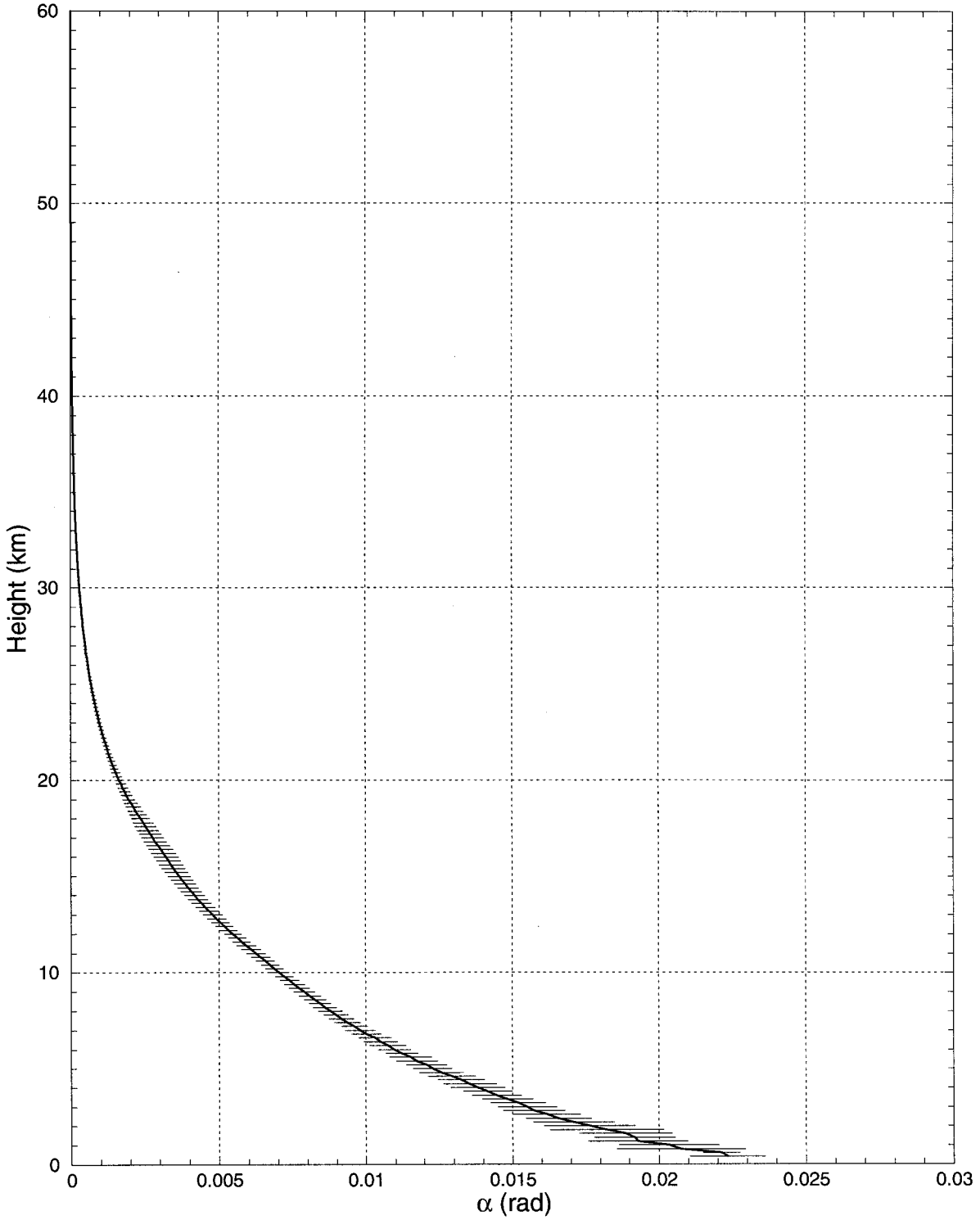

Figure 4. Vertical distribution of the mean (solid curve) and the standard deviations (short lines) of the 62 GPS refraction angle measurements displayed in Figure 2.

where $\vec{\alpha}_l$ and $\vec{\alpha}_l^{\text{obs}}$ are the vectors of the lth simulated and observed refraction angles, respectively.

Figure 4 shows the mean profile of all the GPS refraction angle observations and the standard deviations at different altitudes. We observe that the value of the refraction angle decreases with increasing height in an exponential way. The standard deviation indicates two regions where the refraction angle profiles have a large spread, one near the surface and one in the layer 12–18 km. The large standard deviations near the surface are probably a reflection of large inhomogeneities in temperature and water vapor. The second large standard deviations in the range 12–18 km are probably related to the variation of tropopause at different occultation locations.

The mean differences and the root-mean-square (rms) dif-

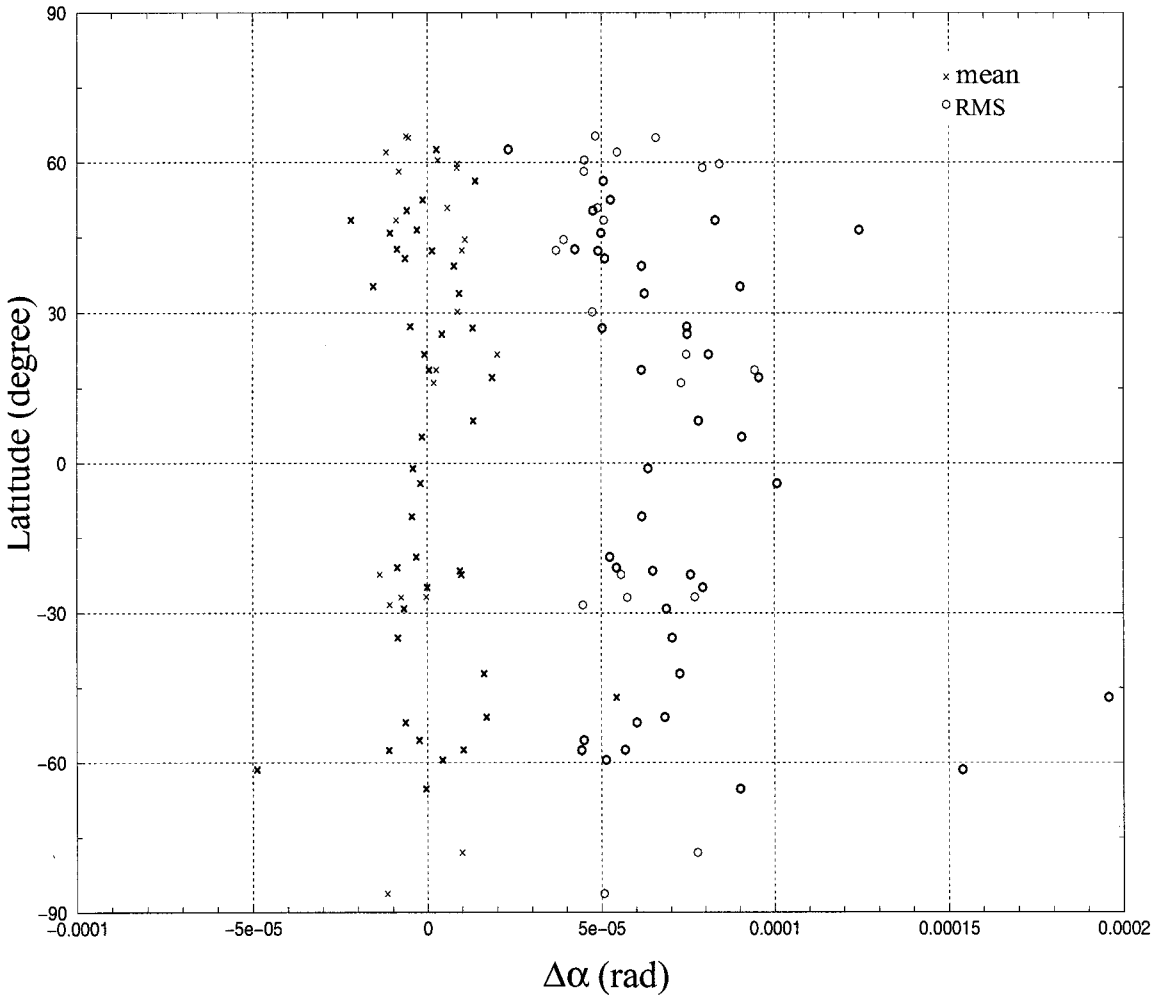

Figure 5. Latitudinal distribution of the mean differences (indicated by crosses) and the rms differences (indicated by circles) between the simulated and the observed refraction angles. The mean and rms differences are calculated over all altitudes above 8 km. The simulated refraction angles are calculated on the basis of the NCEP analysis at 1200 UTC, October 11, 1995.

ferences between the simulated and the observed refraction angles at each occultation location are shown in Figure 5 based on the NCEP analysis at 1200 UTC, October 11, 1995. Because of the limited number of soundings that reached an altitude lower than 8 km, we included only those measurements whose heights are above 8 km. We find that the mean differences are near zero ($<2.5 \times 10^{-5}$ rad) for most of the occultations. The largest mean difference is about 5×10^{-5} (rad) which corresponds to the 33rd GPS occultation. In all cases the mean difference is less than 0.3% of the average total refraction angle, and there are only three soundings whose mean difference is greater than 0.1%. The rms values are less than 0.5%. No obvious latitudinal dependence of the rms differences is found.

We find that soundings with large rms differences occurred mostly 6 hours after the analysis time 1200 UTC, October 11, 1995. To check whether the time difference between the GPS/MET soundings and the NCEP analysis is playing a role in this, we repeated the forward ray tracing for all the GPS occultations using the analysis at 0000 UTC, October 12, and recalculated the mean and rms differences. The results are presented in Figure 6. As in Figure 5, the rms calculation includes only those measurements whose heights are above 8 km. We find that the large rms differences for the three simulated refraction angles based on the NCEP analysis at 1200 UTC, October 11, are greatly reduced using the NCEP analysis at 0000 UTC, October 12. This may suggest that a 6-hour data cutoff window is a better choice than a 12 hour window for incorporating GPS measurements into the numerical forecasting model or a cycling analysis system.

4. Adjoint of Ray-Tracing Operator and Sensitivity Distribution of a Single Observation of Refraction Angle

Having developed the observation operator for GPS refraction angle (section 2), we develop its tangent linear and adjoint of the ray-tracing operator:

Tangent linear operator

$$\mathbf{H}' = \frac{\partial \mathbf{H}(\mathbf{x})}{\partial \mathbf{x}},$$

Adjoint operator

$$\mathbf{H}'^{T}.$$

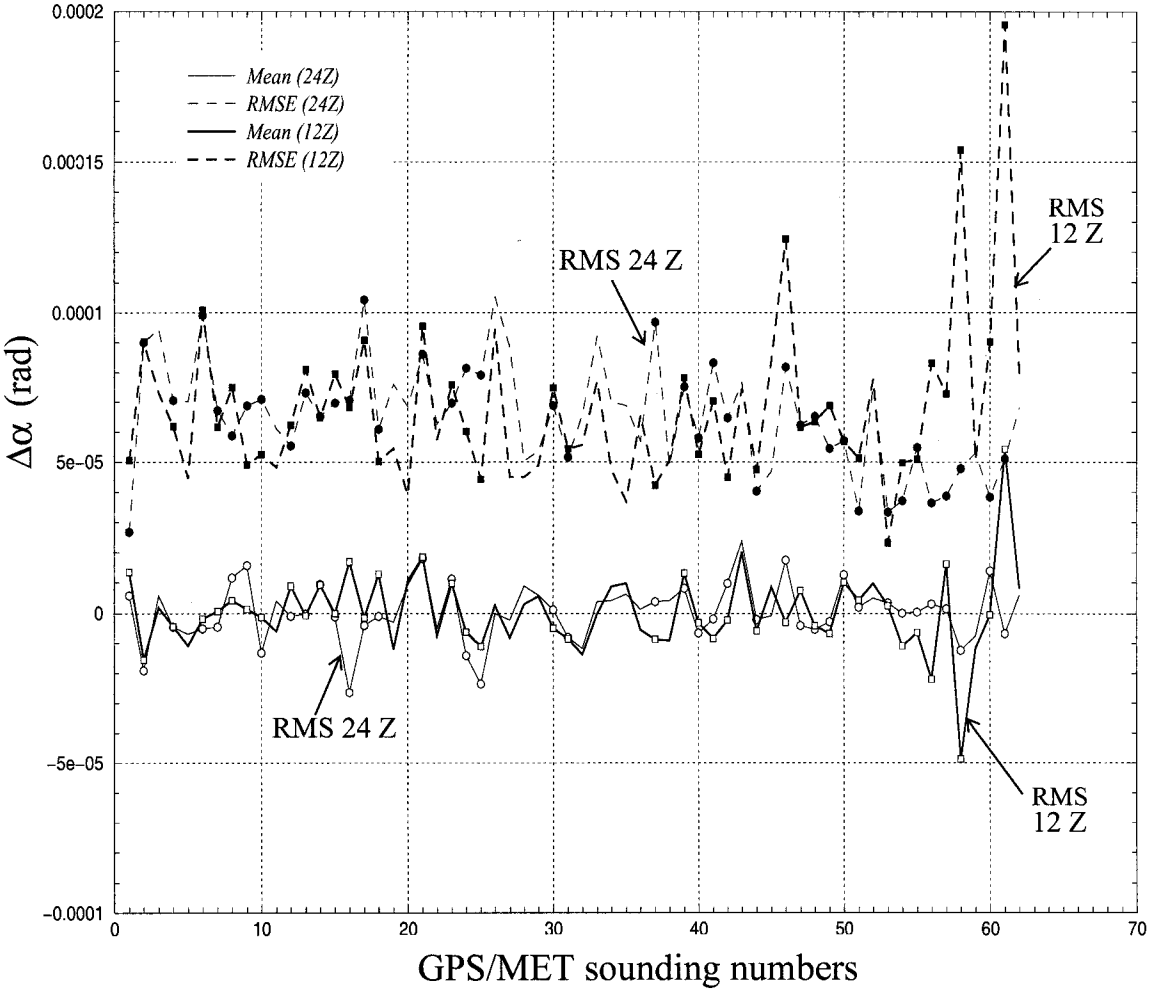

Figure 6. Variation of the mean differences (solid lines) and the rms differences (dashed lines) between the simulated and the observed refraction angles (above 8 km) with respect to the GPS occultation numbers. Thick solid and dashed lines (denoted 12Z) are based on the NCEP analysis at 1200 UTC, October 11, and thin solid and dashed lines (denoted 24Z) are based on the NCEP analysis at 0000 UTC, October 12, 1995. Occultations over ocean are indicated by solid or open circles.

All three GPS operators, $\mathbf{H}$, $\mathbf{H}'$, and $\mathbf{H}'^T$, are required for the use of GPS refraction angles in any variational data analysis/assimilation system.

The development of the tangent linear and adjoint of the ray-tracing operator is carried out at the coding level [*Zou et al.*, 1997]. Notice that in the tangent linear and adjoint model development we do not write the above matrices explicitly. We are only concerned with obtaining the result of a matrix/vector product.

Two methods, a Runge-Kutta method and an alternating direction implicit (ADI) method, were used for solving the ray equation in order to test the computational efficiency. The ADI method is considerably faster than the Runge-Kutta method. Simulation of one GPS occultation with an integration step of 30 km for about 300 rays, using the ADI method, takes about 3, 5, and 18 s CPU times on the Cray C90 at NCEP for the forward ray-tracing $\mathbf{H}(\mathbf{x})$, the tangent linear operator $\mathbf{H}'$, and the adjoint operator $(\mathbf{H}')^T$, respectively. The corresponding costs using the Runge-Kutta method are about 6, 9, and 49 s for $\mathbf{H}(\mathbf{x})$, $\mathbf{H}'$, and $(\mathbf{H}')^T$, respectively.

Having $\mathbf{H}$ and $\mathbf{H}'^T$, we can examine some features of the GPS ray tracing. Theoretically speaking, the refraction angle at one point (perigee point) depends on model state along its entire ray path. As a result, use of a one-point observation of refraction angle in a variational analysis will result in adjustments to model fields over the entire ray path; that is, the influence of one-point GPS measurements will be extended to other regions through the observation operator and its adjoint. To see the effective influence radius in physical space that results from the GPS ray-tracing operator, the sensitivity for a single observation of refraction angle can be examined. Figure 7 shows the sensitivity distribution to the temperature and specific humidity fields for a single refraction angle with 1.385×10^{-3} (rad) observational residual (the difference between simulated and observed refraction angles) at the height of 2.55 km and 58.45°N, 78.12°W, where the sensitivity is measured by the gradient of the squared observational residual. Since the forward ray-tracing operator integrates the ray along the ray trajectory, which goes from one end of the atmosphere to the other, we expect the sensitivities of refraction angle with respect to the model fields to exist along the entire ray. What we find is that the sensitivities along the ray path farther than

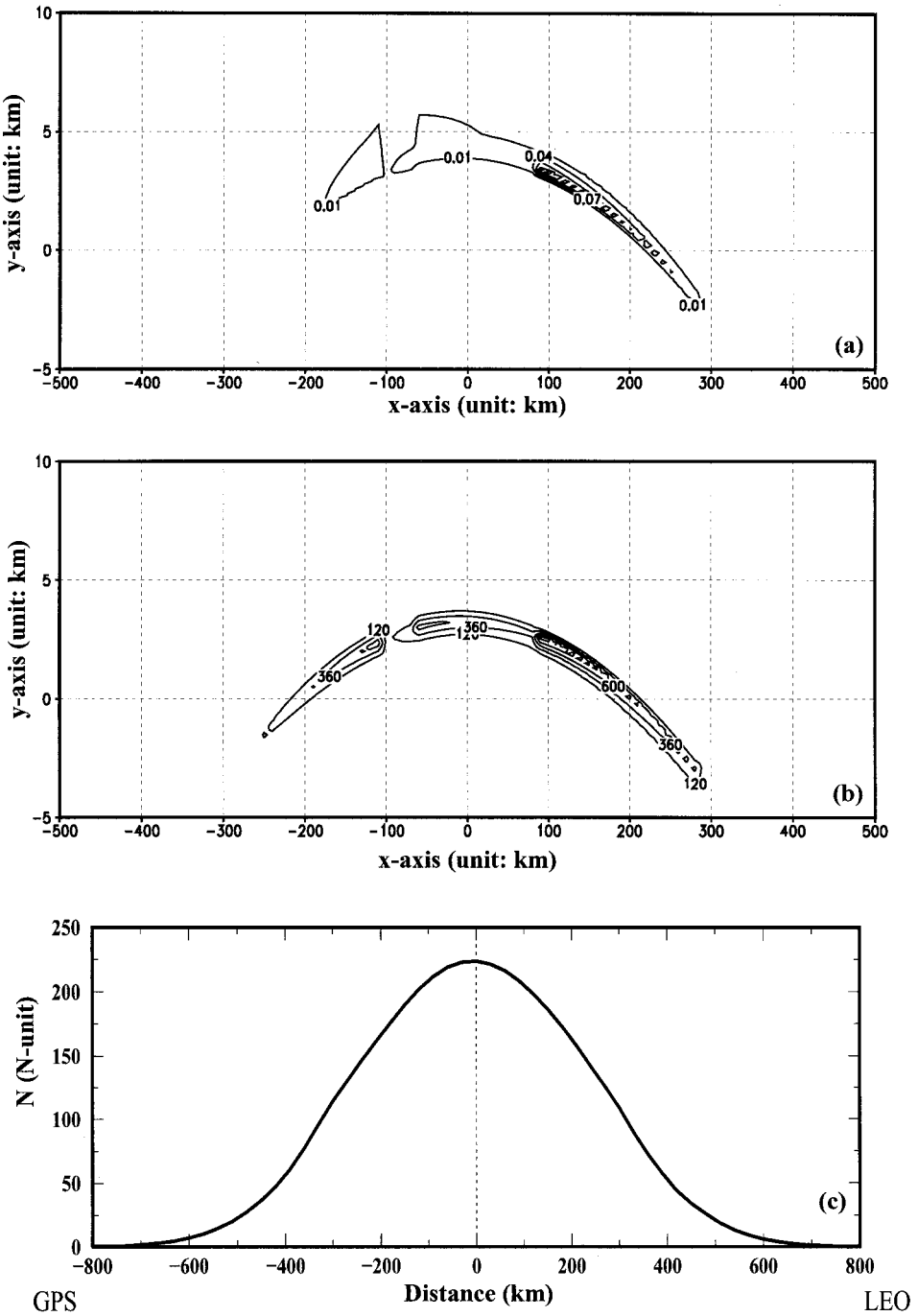

Figure 7. Sensitivity for a single refraction angle at observation at 2.5 km and 58.45°N, 78.12°W in the occultation plane: (a) temperature and (b) specific humidity. The variation of the values of refractivity along the ray trajectory is plotted in Figure 7c. The perigee point corresponds to $x = 0$ in the x-y coordinate in the occultation plane. The ray comes from the left and goes away from the right. Contour intervals for Figures 7a and 7b are 0.03 K^{-1} and 240 $(g/kg)^{-1}$.

300 km away from the perigee points exist but are much smaller (by 2 orders of magnitude) than the sensitivities within ±300 km from the perigee points (Figures 7a and 7b). The maximum sensitivities for both the temperature and the specific humidity are located in the right-hand side (LEO side) of the perigee point. This could be related to the fact that the ray bends downward toward large refractivity values, which occurs mostly in the LEO side of the perigee point of the ray since the atmospheric refractivity decreases with height. The sensitivity patterns show an elongated circular shape, following the contour lines of refractivity in the same occultation plane (figure omitted). The value of the atmospheric refractivity (N^{LOC}) along the ray is plotted in Fig. 7c, which shows a distribution of parabolic shape with a much reduced value of N^{LOC} (nearly zero) 600 km away from the perigee point. The increase of N^{LOC} from −600 km to 0 km (the perigee point position)

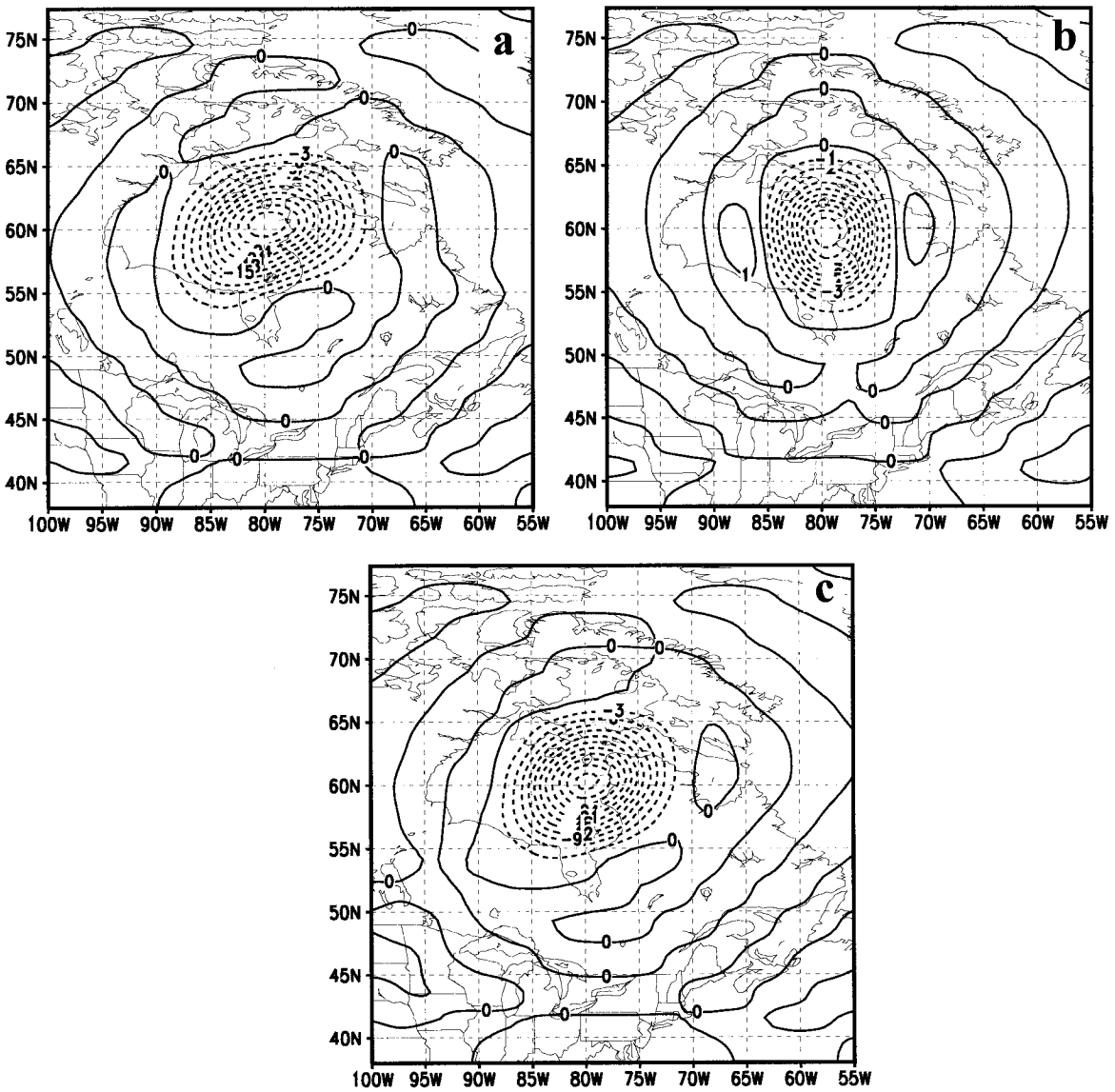

Figure 8. Sensitivity of the cost function J (see equation (13)) with respect to the (a) temperature (T), (b) specific humidity (q) on $\sigma = 0.535$ level, and (c) pressure fields (P). The values of the sensitivity are multiplied by a constant of -2.192×10^{-7}. Labels in Figures 8a, 8b, and 8c (c) are scaled by 10^2, 10^2, and 10^3, respectively. Contour intervals for T, q, and P are 0.03 K^{-1}, 0.01 $(kg/kg)^{-1}$, and 0.03 hPa^{-1}.

reflects the ray coming into the atmosphere, and the decrease of N^{LOC} from 0 km to 1000 km corresponds to the ray leaving the atmosphere.

One occultation produces hundreds of rays. These rays usually have different occultation planes (with slightly different normal directions). Given the influence radius of about 600 km of the refraction angle along the ray path and the fact that the vertical scale is much smaller than 600 km, a single model level may be affected by all the rays of one occultation. What will the sensitivity distribution look like on model σ levels? Let us define a cost function

$$J(x) = (\vec{\alpha} - \vec{\alpha}^{obs})^T \mathbf{W} (\vec{\alpha} - \vec{\alpha}^{obs}) \quad (13)$$

which measures the distance (in a least square sense) between simulated and observed refraction angles for GPS-1. W is a diagonal weighting matrix approximated by the inverse of the mean square differences between the simulated and the observed refraction angles, including all the 62 GPS soundings. Figure 8 shows the distributions of the gradient (∇J) with respect to the temperature and the specific humidity at $\sigma = 0.535$ and the surface pressure. We observe that large sensitivities occur not only at the occultation location but also over a nearly circular area of about 600 km $\times$ 600 km centered at the perigee point. Adjustments farther away from the perigee points exist but are much smaller than the sensitivities near the perigee points. An example is given in Figure 9, which is the same as Figure 8a except over the entire globe with a smaller value of contour interval. The sensitivity distribution reflects the collective effect of all the ray paths for GPS-1 on the model state. Although sensitivities exist over the entire globe, the value of the sensitivity drops 2 orders of magnitude about 600 km away from the perigee point.

Keeping these ray-tracing-induced structures in mind is important for the interpretation of the analysis increment from

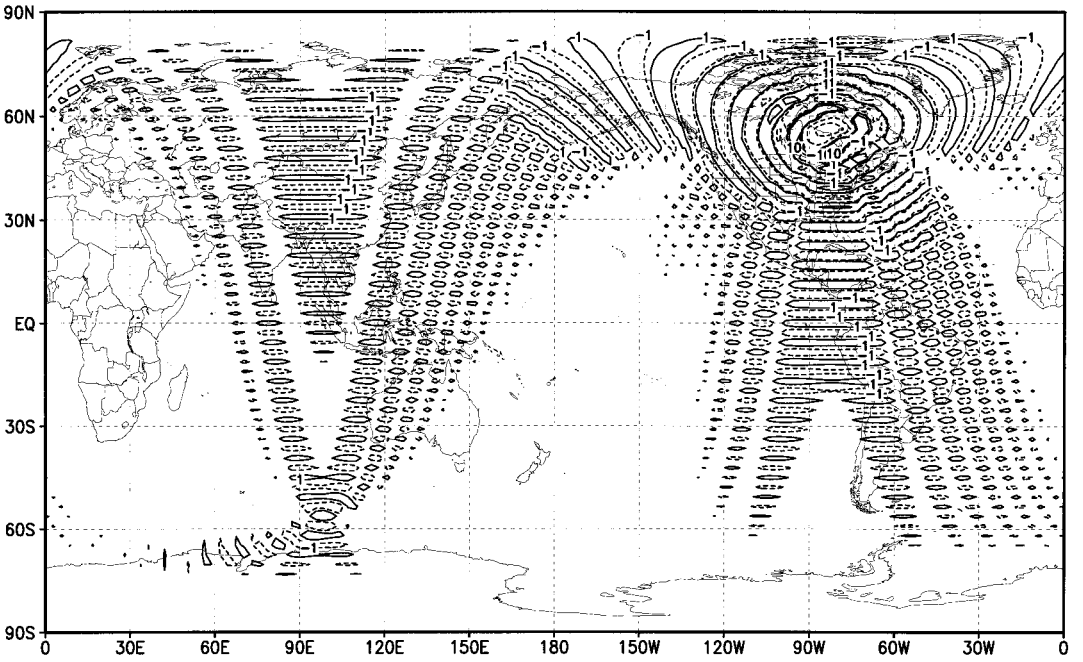

Figure 9. Same as Fig. 8a but for the entire globe. Labels are scaled by 10^3. Contours plotted are -300, -100, -10, -1, 1, 10, 100, 300 K^{-1}.

the use of GPS refraction angle. The horizontal scale analysis increments with the use of GPS refraction angles will be broader than that purely from the background error covariances seen in a traditional single observation experiment [*Courtier et al*., 1998].

5. GPS Refraction Angle and Refractivity and Their Use for Data Analysis

In terms of temperature (T), specific humidity (q), and pressure (P) the refractivity N can be written as [*Bean and Dutton*, 1968]

$$N = 10^6(n - 1)$$

$$= 77.6\,\frac{P}{T} + 3.73 \times 10^5\,\frac{P_q}{T^2(0.622 + 0.378q)}. \qquad (14)$$

Therefore for a given atmospheric state of T, q, and P on a model grid, the atmospheric refractivity N can be calculated through (14). We will denote this refractivity as N^{local} to be more specific and call it either the local atmospheric refractivity or the atmospheric refractivity. The first term in (14) will be denoted as $N^{\text{local}}_{\text{dry}}$ and the second term as $N^{\text{local}}_{\text{wet}}$ (Table 1).

Examples of how N^{local}, $N^{\text{local}}_{\text{dry}}$, and $N^{\text{local}}_{\text{wet}}$ are distributed over the globe are shown in Figure 10. Figure 10a shows the global distribution of N^{local} at 850 hPa based on NCEP analysis at 1200 UTC, October 11, 1995. To show the refractivity variations more clearly, the global mean of the refractivity field is subtracted from N. Large values of refractivity are found to concentrate in the tropical region between 30°N and 30°S, with a longitudinal distribution similar to the specific humidity field (figure omitted). Minimum values of refractivity (see dashed line regions) found over the regions of the Himalaya Mountains, Rocky Mountains, South America, Greenland, and the South Pole are not realistic and have resulted from the high terrain at these locations, and the surface pressure is lower than 850 hPa. They mostly represent the features in the temperature and pressure fields. Such a correlation is seen more clearly when we separate N^{local} into $N^{\text{local}}_{\text{dry}}$ (Figure 10b) and $N^{\text{local}}_{\text{wet}}$ (Figure 10c). From these figures we conclude that large gradients of atmospheric refractivity N^{local} exist near the boundaries between moist air in the tropical regions and dry air in midlatitudes.

In the upper troposphere (300 hPa, Figure 11), N^{local} is dominated by the dry term $N^{\text{local}}_{\text{dry}}$. The largest values of $N^{\text{local}}_{\text{wet}}$ appear in the tropical regions, but their magnitudes are smaller than $N^{\text{local}}_{\text{dry}}$ by about 2 orders of magnitude.

The values of N^{local} shown in Figures 10 and 11 are atmospheric refractivity values calculated from the gridded temperature, specific humidity, and pressure fields. N^{local} is different from N^{GPS} derived from (2). The size of such a difference depends on the variation of N^{local} along the ray path near the perigee point. Theoretically speaking, the larger the horizontal gradients of N^{local} the bigger the differences. Assessment of such a difference between N^{local} and N^{GPS} can be made by comparing N^{local} with N^{GPS} (calculated on the basis of the same analysis), where N^{local} is calculated through (14) from the gridded analysis of T, q, and P and interpolated to the GPS occultation locations, and N^{GPS} is calculated by first computing the simulated refraction angle using the ray-tracing algorithm

Table 1. Mathematical Symbols Used for Atmospheric Refractivity Derived Differently

Refractivity	Brief Description
N, or N^{local}	equation (14)
$N^{\text{local}}_{\text{dry}}$	$77.6\,(P/T)$
$N^{\text{local}}_{\text{wet}}$	$3.73 \times 10^5\,(P_q/T^2(0.622 + 0.378q))$
N^{GPS}	ray tracing + Abel inversion
N^{obs}	observed refraction angle plus Abel inversion

(section 2) and then using the Abel inversion to derive N^{GPS}. Figure 12 shows the mean of the difference $N^{GPS} - N^{local}$, averaged over a total of 62 soundings based on the NCEP analysis, at 1200 UTC, October 11 (dotted line) and 0000 UTC (solid line), October 12, 1995. We find that the difference between N^{GPS} and N^{local} is relatively small (less than 1 N-unit). A small negative N-bias is observed in the upper troposphere (4–10 km), and positive N-bias appears below and above the negative N-bias region. Since Figure 12 is computed only from model data and is not related to the GPS/MET real data, it is likely that these errors, although small, are caused by the nonlinear nature of the problem and its approximated solution (by Abel inversion).

Although the mean difference between N^{GPS} and N^{local} is small, the value of $N^{GPS} - N^{local}$ can be large for some individual soundings. Figure 13 plots a "spaghetti" map showing the vertical profiles of $N^{GPS} - N^{local}$ for all the GPS soundings that occurred during 1200 UTC, October 11, and 0000 UTC, October 12, 1995, based on the NCEP analysis at 1200 UTC, October 11, 1995. A few large differences whose absolute values are greater than 5 or 10 N-units are found in the lower troposphere.

We plot in Figure 14 the differences of $N^{local} - N^{obs}$ (solid line), $N^{GPS} - N^{obs}$ (dashed line), and $N^{GPS} - N^{local}$ (dotted line) for GPS-1 (Figure 14a) and GPS-32 (Figure 14b) based

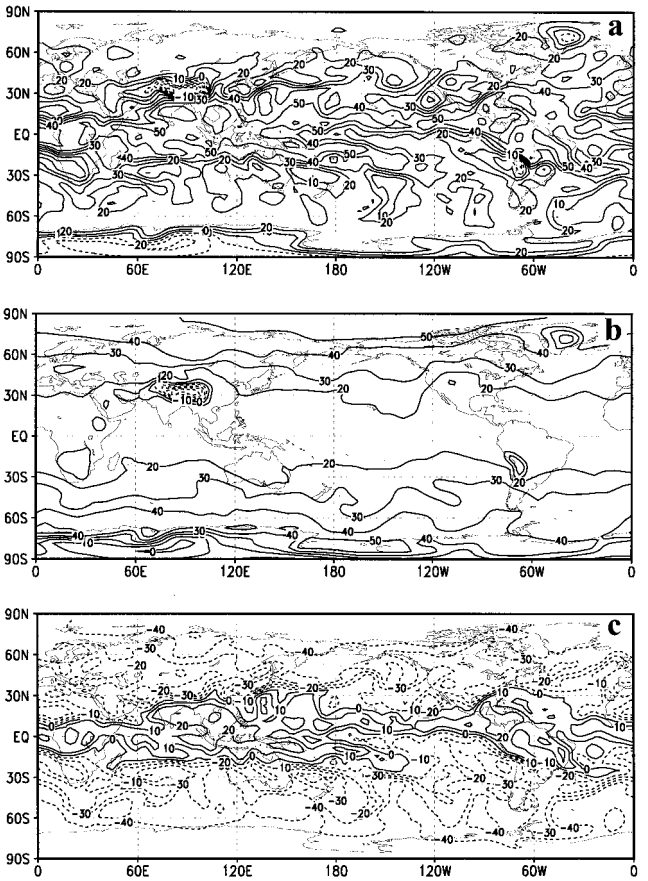

Figure 10. Global distribution of (a) ($N^{local} - \bar{N}^{local}$), (b) ($N^{local}_{dry} - \bar{N}^{local}_{dry}$), and (c) ($N^{local}_{wet} - \bar{N}^{local}_{wet}$) at 850 mbar based on the NCEP analysis at 1200 UTC, October 11, 1995, where $\bar{N}^{local} = 240$, $\bar{N}^{local}_{dry} = 210$, *and* $\bar{N}^{local}_{wet} = 50$ N-units are the global average of N^{local}, N^{local}_{dry}, and N^{local}_{wet}, respectively. Contour interval is 10.0 N-units.

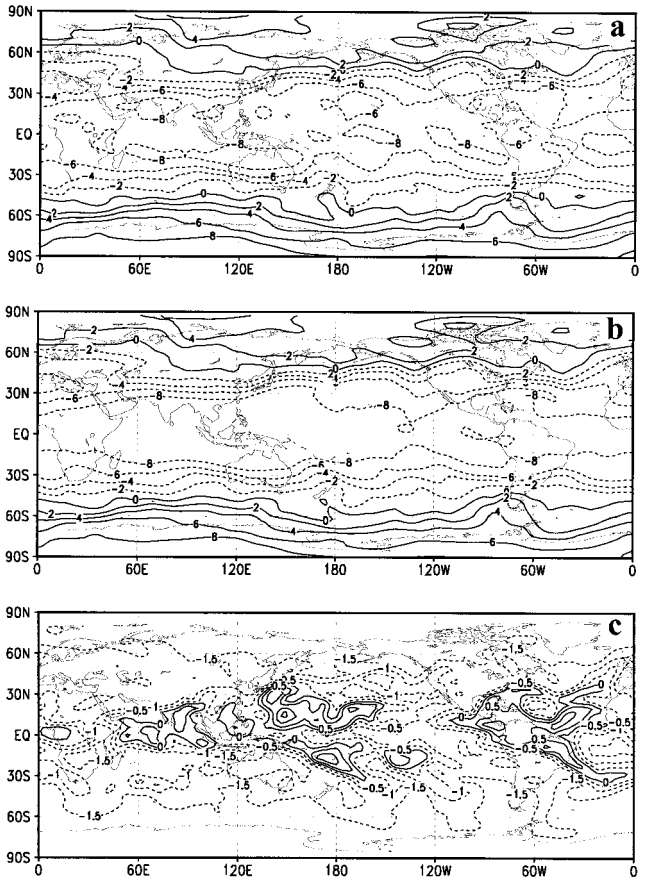

Figure 11. Same as Figure 7 except at 300 mbar. $\bar{N}^{local} = 104$, $\bar{N}^{local}_{dry} = 104$, and $\bar{N}^{local}_{wet} = 1.7$. Contour intervals in Figures 7a, 7b and 7c are 2.0, 2.0, and 0.5 N-units, respectively.

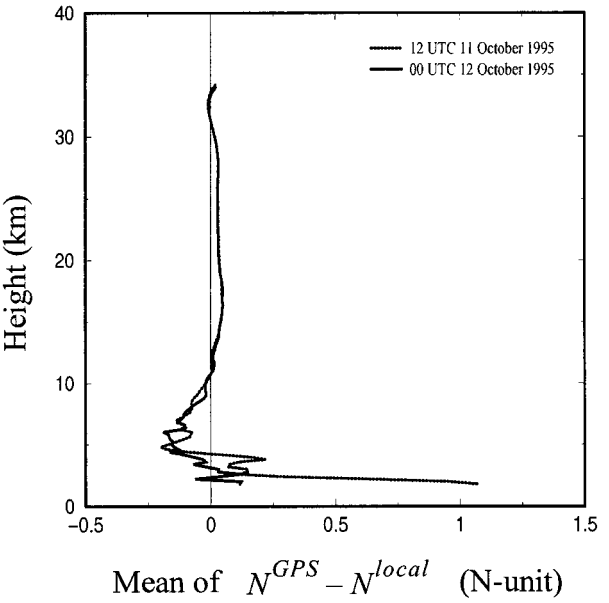

Figure 12. Difference of N^{GPS} and N^{local} averaged over all the 62 soundings based on the NCEP analysis at 1200 UTC, October 11 (dotted line), and 0000 UTC, October 12, 1995 (solid line), respectively.

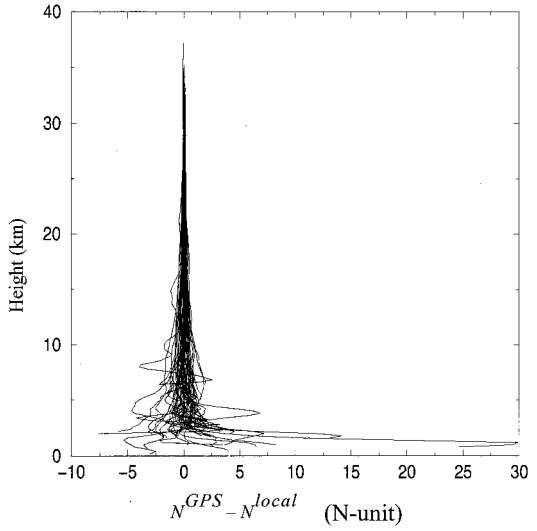

Figure 13. A "spaghetti" map showing the 62 vertical profiles of the differences of $N^{\mathrm{GPS}} - N^{\mathrm{local}}$. Both N^{GPS} and N^{local} are calculated on the basis of NCEP analysis at 1200 UTC, October 11, 1995.

on the NCEP analysis at 1200 UTC, October 11, 1995. We find from Figure 14a that (1) the local atmospheric refractivity N^{local} is different from the GPS-derived refractivity N^{GPS}; (2) the differences between $N^{\mathrm{local}} - N^{\mathrm{obs}}$ and $N^{\mathrm{GPS}} - N^{\mathrm{obs}}$ are similar in their vertical structures; and (3) the errors introduced by the approximation of N^{local} by N^{GPS} are positive for GPS-1 and negative for GPS-32 and, in general, smaller than the analysis errors $N^{\mathrm{GPS}} - N^{\mathrm{obs}}$. These results show that the GPS-derived refractivity measurements can sometimes, but not always, be used as if they were a local refractivity profile. For example, the errors introduced by the local spherical symmetry assumption used in the GPS-derived refractivity for the 32nd GPS occultation (GPS-32) are as small as the analysis differences for that sounding GPS-32 (Figure 14b). Comparing Figure 2 (the sounding locations) with Figure 10 (the refractivity distribution), we find that this occultation occurs over a region with a large refractivity gradient. The fact that the differences between N^{GPS} and N^{local} may be large should be considered if the GPS-derived refractivity data are used directly for data retrieval (such as the dry-temperature retrieval) and other research applications.

For GPS measurements we face a decision as to what to incorporate into a data analysis and/or assimilation system: α, N^{GPS}, or T^{dry} and P^{dry} (retrieved under dry atmosphere assumption)? We can propose four different approaches for GPS data analysis and/or assimilation: (1) use of GPS refraction angle which includes a quadratic term of

$$(\vec{\alpha}(\mathbf{x}) - \vec{\alpha}^{\mathrm{obs}})^T \mathbf{W}_{\alpha}(\vec{\alpha}(\mathbf{x}) - \vec{\alpha}^{\mathrm{obs}}) \tag{15}$$

in the cost function J minimized in a 3DVAR and/or 4DVAR system; (2) use of GPS refractivity with its observation operator consistent with its measurements, i.e., including in J the following quadratic term:

$$(\vec{N}^{\mathrm{GPS}}(\vec{\alpha}(\mathbf{x})) - \vec{\mathbf{N}}^{\mathrm{obs}})^T \mathbf{W}_{N^{\mathrm{GPS}}}(\vec{N}^{\mathrm{GPS}}(\vec{\alpha}(\mathbf{x})) - \vec{\mathbf{N}}^{\mathrm{obs}}); \tag{16}$$

(3) use of GPS refractivity with an approximated observation operator, i.e., including in J the following quadratic term:

$$(\vec{N}^{\mathrm{local}}(\mathbf{x}) - \vec{\mathbf{N}}^{\mathrm{obs}})^T \mathbf{W}_{N^{\mathrm{local}}}(\vec{N}^{\mathrm{local}}(\mathbf{x}) - \vec{\mathbf{N}}^{\mathrm{obs}}); \tag{17}$$

(4) use of the GPS-retrieved products such as temperature, pressure, and geopotential height, or specific humidity given an independent estimate of temperature.

For approach 2 we not only need to develop and run the ray tracing and the adjoint of the ray tracing (same as for approach 1) but also the Abel inversion and the adjoint of the Abel inversion. The approach 2 scheme is thus a less favorable choice than approach 1 since the observation operator in approach 2 is computationally more expensive, and the observational error covariance matrix must contain errors introduced in the Abel inversion. Method 3 is theoretically superior to 4 since method 4 contains more retrieval error sources than method 3. The a priori separation of contributions from the dry and moist atmosphere to the refractivity is not needed in method 3. The difference in the computational expense between methods 3 and 4 is small. Therefore the two strategies

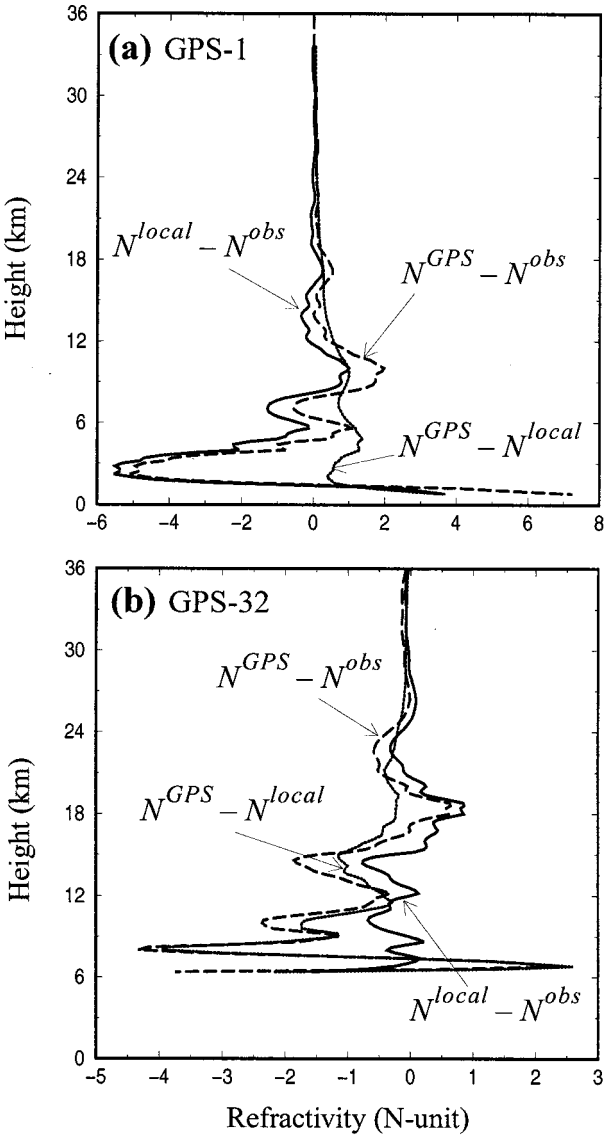

Figure 14. Differences of $N^{\mathrm{local}} - N^{\mathrm{obs}}$ (solid line), $N^{\mathrm{GPS}} - N^{\mathrm{obs}}$ (dashed line), and $N^{\mathrm{GPS}} - N^{\mathrm{local}}$ (dotted line) for (a) GPS-1 and (b) GPS-32. Both N^{local} and N^{GPS} are calculated on the basis of NCEP analysis at 1200 UTC, October 11, 1995.

for GPS data analysis/assimilation which are most promising are methods 1 and 3. In method 1 the observation operator simulates the GPS refraction angle accurately and the error characteristics are simpler. However, method 1 involves a numerical integration of the ray equation along the ray path for each ray. Simulation of one GPS occultation may contain several hundred rays, depending on the vertical resolution, the height of the model top, and the height of the perigee point when the ray intersects the Earth. For example, GPS sounding 34 contains 258 rays and GPS sounding 25 contains 298 rays, given a vertical resolution of 0.2 km (which is used for the present study). Strategy 3 is not so good as 1, as far as the compatibility between the simulated and the observed data and the specification of the observation error covariances are concerned. However strategy 3 is computationally much cheaper than 1. Method 3 might work well if the differences between N^{local} and N^{GPS} are much smaller than the differences between N^{GPS} and N^{obs}, or if the errors resulting from the local spherical symmetry approximation can be properly included in the observational error covariances used in the analysis/assimilation systems.

Another possibility to consider is a combined analysis/assimilation strategy: to assimilate refraction angles in the lower troposphere where $|N^{\text{local}} - N^{\text{GPS}}|$ is large and to switch to refractivity in the upper troposphere and stratosphere where $|N^{\text{local}} - N^{\text{GPS}}|$ is small. Such an approach will not only save CPU time because of the reduced numbers of ray tracings but will also minimize the effects of errors contained in the refraction angle calculation near and above the top of the model, because of its dependence on the vertical extrapolation and CIRA data [*Rees et al*., 1990] rather than on the atmospheric state. Assimilation of the retrieved refractivity near the model top overcomes this problem.

6. Summary and Conclusions

Several previous studies have indicated that the GPS measurements are of good quality and possess the potential to add valuable information to global analysis and prediction. These studies were based on the comparison between derived GPS products (temperature, water vapor, and geopotential heights) and other types of data (operational global analysis, radiosondes, and radiometric soundings). However, the impact of GPS measurements on operational analyses and forecasts has not yet been assessed through a direct use of GPS/MET refraction angle data. This paper presents the first step toward incorporating the GPS "raw" measurements into a numerical weather analysis and forecast system.

A forward ray-tracing observation operator, which calculates the refraction angles for a given atmospheric state, is described. Comparison is made between the simulated refraction angles using this operator on the NCEP analysis and the real GPS-measured refraction angle data. The simulated GPS refraction angles, based on the NCEP analysis, differ from the GPS/MET observation by about 5–10% for most of the occultations in certain altitudes below 20 km.

The tangent linear and adjoint of the ray-tracing operator are developed and used for conducting a sensitivity study of a single observation of refraction angle. Numerical results indicate that the use of a single refraction angle in a variational analysis results in perturbation of meteorological fields of temperature, specific humidity, and pressure along its ray path, with significant changes occurring only in an elongated band of ± 300 km following the ray path in the occultation plane. Use of all the refraction angles of one occultation (including all the rays in the vertical) generated major adjustments to the model state in an area of about 600 km $\times$ 600 km large on model σ-levels, centered around the ray perigee point. These structures represent unique features of the observation operator of GPS refraction angles. Adjustments in the model state, when combined with a background term, will be extended to a larger area and to wind fields under the influence of the background error covariances.

In the distributions of atmospheric refractivity fields, large gradients of atmospheric refractivity exist near the boundaries separating the moist tropical air from the dry midlatitude air. Comparing the simulated GPS refractivity, the local atmospheric refractivity, and the GPS measurement-derived refractivity, we found that for many soundings the local atmospheric refractivity N^{local} is close to the GPS-derived refractivity N^{GPS}. Differences between these two are much smaller than the differences between the analyzed and the observed N^{GPS} for most of the soundings. For soundings located over regions where the refractivity gradient is large, errors introduced by spherical symmetry assumption cannot be neglected. In such cases the direct use of GPS refraction angle measurements is required to eliminate the potentially large errors introduced by the use of GPS refractivity.

7. Appendix

A1. Deriving α and p From Doppler Shift

The basic GPS measurement is the phase shift against time. Each time a LEO rises and sets on its 730 km orbit, relative to one of the 24 operational GPS satellites, the GPS receiver on the LEO is in position to sense the radio signals emitted from the GPS. On their way from the GPS to the LEO, the radio waves transect successive layers of the Earth's atmosphere and are bent before they reach the receiver due to atmospheric refraction. The LEO receiver tracks in time the phase delays caused by the bending and slowing of these radio signals. The associated phase path s, i.e., phase delay multiplied by the wavelength, is equal to

$$s = \int_{\text{GPS}}^{\text{LEO}} n \, dl, \tag{A1}$$

where n is the index of refractivity and l is the abscissa along the ray path. From this time series the Doppler frequency shift f_d can be estimated for both carrier frequencies f_c (1227.6 and 1575.42 MHz) through the relation

$$f_d = -f_c c^{-1} \frac{ds}{dt}, \tag{A2}$$

where c is the light velocity in a vacuum (the use of two radio frequencies permits the removal of ionospheric effects).

On the other hand, the carrier frequency Doppler shift f_d is related to the satellites geometry by the expression

$$f_d = f_c \left(\frac{c - n_L \vec{v}_L \cdot \vec{u}_L^t}{c - n_G \vec{v}_G \cdot \vec{u}_G^t} - 1 \right), \tag{A3}$$

where the subscripts "G" and "L" stand for the GPS and the LEO satellite, $\vec{v}_{G,L}$ are the satellite velocity vectors, $\vec{u}_{G,L}^t$ are the unit vectors representing the tangent directions of the ray

at the GPS and the LEO satellite locations, and $n_{G,L}$ are the refractivity indices at satellite locations. Satellite velocities can be decomposed as follows:

$$\vec{v}_{G,L} = \vec{v}^{n}_{G,L} + \vec{v}^{r}_{G,L} + \vec{v}^{t}_{G,L}, \tag{A4}$$

where $\vec{v}^{n}_{G,L}$ is a component normal to the ray plane (i.e., defined by GPS, LEO satellite, and the Earth's center), and $\vec{v}^{r}_{G,L}$ and $\vec{v}^{t}_{G,L}$ are radial and tangent components in the ray plane. Introducing $\phi_{G,L}$ to represent the angle between the satellite radii $\vec{r}_{G,L}$ and the unit vectors $\vec{u}^{t}_{G,L}$, which are called ray zenith angles, the expression for the Doppler shift can be written as

$$f_d = f_c \left(\frac{c - n_L(v^r_L \cos \phi_L - v^t_L \sin \phi_L)}{c - n_G(v^r_G \cos \phi_G - v^t_G \sin \phi_G)} - 1 \right). \tag{A5}$$

In equation (A5), c and f_c are known, $\vec{v}_{G,L}$ can be very accurately measured using the other satellites of the GPS constellation, and f_d can be deduced from the frequency Doppler shift (equation (A1)). The only two unknown variables are $\phi_{G,L}$. Thus radio occultation measurements provide a relation linking the two satellite zenith angles ϕ_G and ϕ_L but do not suffice to determine the values of both ϕ_G and ϕ_L.

A second relation between ϕ_G and ϕ_L can be added by assuming that the impact parameter p has the same value at the GPS and LEO satellite positions; that is,

$$p = r_G n_G \sin \phi_G = r_L n_L \sin \phi_L. \tag{A6}$$

As the satellite radii $\vec{r}_G$ and $\vec{r}_L$ and velocities $\vec{v}_G$ and $\vec{v}_L$ are precisely known, we now have two equations (A5) and (A6) for two unknowns ϕ_G and ϕ_L. An iterative method can then be used to solve for ϕ_G and ϕ_L. Convergence is generally obtained after a few iterations [*Gorbunov et al*., 1996].

When ϕ_G and ϕ_L are known, both the impact parameter p and the refraction angle α can be estimated from them using the following relationships:

$$p = r_G n_G \sin \phi_G \tag{A7}$$

$$\alpha = \phi_G + \phi_L + \arccos\left(\frac{\vec{r}_G \vec{r}_L}{r_G r_L}\right) - \pi. \tag{A8}$$

The equations (A5)–(A8) are solved for α and p separately for each of the two GPS carrier frequencies, assuming that $n_G \leq n_L = 1$. This introduces error for each frequency because LEO satellite is inside the ionosphere. However, this error is removed or significantly reduced after the ionosphere correction (i.e., a linear combination) of the bending angles [*Vorob'yev and Krasil'nikova*, 1994].

A2. Calculating the Geodetic Coordinates (z, φ, λ) From Local Cartesian Coordinates (x_1, x_2, x_3)

When performing ray tracing, we need to calculate refractivity and its gradient in given Cartesian coordinates. To do this, we need to convert Cartesian coordinates (x_1, x_2, x_3) to geodetic altitude, latitude, and longitude (z, φ, λ) for the model-gridded fields. Since calculation of longitude is not a problem, we consider calculation of z and φ below. According to *Runcorn* [1967], geodetic altitude z of the point (x^*_1, x^*_2) is the distance from this point to the reference ellipsoid, i.e., the distance along a direction normal to the reference ellipsoid, and the geodetic latitude is an angle between this direction and the x axis (not polar angle). Using the equation of ellipse,

$$\frac{x_1^2}{R_e^2} + \frac{x_2^2}{R_p^2} = 1, \tag{A9}$$

where $R_e = 6378.1363$ km and $R_p = 6356.7516$ km are equatorial and polar radii, and equation of the line normal to ellipse,

$$\frac{x^*_2 - x_2}{x^*_1 - x_1} = \frac{R_e^2 x_2}{R_p^2 x_1}, \tag{A10}$$

we obtain the set of two equations to solve for two unknowns (x_1, x_2). Since it may not be solved analytically, iterative technique is applied. After (x_1, x_2) are solved with required accuracy, we can derive z and φ:

$$z = \sqrt{(x^*_1 - x_1)^2 + (x^*_2 - x_2)^2}, \tag{A11}$$

$$\varphi = \operatorname{arctg} \frac{R_e^2 x_2}{R_p^2 x_1}. \tag{A12}$$

To reduce CPU time for ray tracing by avoiding the iterative technique to solve (A9) and (A10), we use the following approximate equation:

$$\frac{x^*_2 - x_2}{x^*_1 - x_1} = \frac{R_e^2 x^*_2}{R_p^2 x^*_1}, \tag{A13}$$

instead of the exact one (A10). This allows us to obtain an analytical solution:

$$z = \sqrt{(x^*_1)^2 + (x^*_2)^2} \left(1 - \frac{R_e^2 R_p^2}{\sqrt{R_e^2 (x^*_2)^2 + R_p^2 (x^*_1)^2}} \right), \tag{A14}$$

$$\varphi = \operatorname{arctg} \frac{R_e^2 x^*_2}{R_p^2 x^*_1}, \tag{A15}$$

which provides an accuracy for z of a few meters in the altitude range of 0–35 km.

A3. Calculating N and ∇N in Cartesian Coordinates From Model State of T, q, and p_s (Surface Pressure)

Calculation of the refractivity N and its gradient ∇N at an arbitrary point in Cartesian coordinates is based on an interpolation scheme described in the following.

The values of the temperature T_{ijk} and specific humidity q_{ijk} are given for the Gaussian grid of the latitudes φ_j, the homogeneous grid of the longitudes λ_k, and an irregularly spaced grid of heights z_{ijk}, described below. For T62 resolution of the NCEP spectral model, the indices have the following ranges: $i = 1, \ldots, 28$, $j = 1, \ldots, 64$, $k = 1, \ldots, 128$.

The values of the pressure corresponding to the ith levels are calculated as follows [*Sela*, 1980]:

$$P_{ijk} = \sigma_i P_{s,jk}, \tag{A16}$$

where $P_{s,jk}$ is the surface pressure for the jth latitude and kth longitude, and σ_i is the vertical coordinate parameter.

Calculation of the geopotential heights was based on the formula [*Sela*, 1980]

$$\Phi_{i-1,jk} - \Phi_{ijk} = \frac{c_p}{2} \left[T_{v,i-1,jk} \left(\frac{\pi_{ijk}}{\pi_{i-1,jk}} - 1 \right) + T_{v,ijk} \left(1 - \frac{\pi_{i-1,jk}}{\pi_{ijk}} \right) \right] \qquad \pi_{ijk} = P_{ijk}^{R_d/c_p}, \tag{A17}$$

where R_d is the gas constant for the dry air, c_p is the specific heat at constant pressure, $T_{v,ijk} = T_{ijk}\ (1 + (R_v/R_d - 1)\ q_{ijk})$ is the virtual temperature, R_v is the gas constant for the water vapor, and $\Phi_{1,jk} = \Phi_{s,jk}$ is the surface geopotential (orography).

Given the temperature, pressure, and humidity at a grid point, the corresponding value of the refractivity N ($N = 10^6(n - 1)$) was calculated by means of the formula [*Bean and Dutton*, 1968]

$$N_{ijk} = 1 + c_1 \frac{P_{ijk}}{T_{ijk}} + c_2 \frac{P_{w,ijk}}{T_{ijk}^2}, \tag{A18}$$

$$P_{w,ijk} = \frac{q_{ijk} P_{ijk}}{\dfrac{R_d}{R_v} + \left(1 - \dfrac{R_d}{R_v}\right) q_{ijk}}, \tag{A19}$$

where $P_{w,ijk}$ is the water vapor pressure (in hectopascals), and the constants $c_1 = 7.76 \times 10^{-5}$ K hPa-1, $c_2 = 0.373$ K^2 hPa-1.

To relate the gridded value of the refractivity to a spatial location, we used the reference ellipsoid model with the semiaxes being equal to 6378.1363 and 6356.7516 km and the corresponding gravity field distribution $g(z, \varphi, \lambda)$ [*Lambeck*, 1988], where z is the height above the Earth's surface. Calculation of the geometrical heights z_{ijk} was based on the definition of the geopotential

$$\Phi_{ijk} = \int_0^{z_{ijk}} g(\zeta, \varphi_j, \lambda_k)\, d\zeta. \tag{A20}$$

For every Φ_{ijk}, this equation was numerically solved for the corresponding z_{ijk} (Appendix, section A4).

Then refractivity was interpolated vertically by cubic splines and linearly with respect to the φ, λ coordinates. Interpolation of refractivity N is performed on the logarithm of N. For calculation of the vertical component of the gradient of refractivity, the derivative of the spline with respect to the z coordinate was linearly interpolated with respect to the φ, λ coordinates.

The gridded index of refractivity is given in the height range of about 0–35 km. However, accurate calculation of the total bending of the ray requires knowledge of the refractivity up to a height of 120 km. In the height range 35–120 km, where we have no NCEP data, we used the index of refractivity calculated from the CIRA (Committee on Space Research (COSPAR) International Reference Atmosphere) model. (The CIRA model is a middle-atmosphere model described by *Rees et al.* [1990] and is presented as tabulations of atmospheric properties (temperature, pressure, and zonal wind), as functions of latitude, pressure or geometric height, and time of year. These are data obtained from various observational instruments.) To have a smooth transition from the exponentially extrapolated gridded index of refractivity n_{NCEP} to that from the CIRA model n_{CIRA}, we used the following formula:

$$n(z) = (n_{\mathrm{NCEP}}(z) - n_{\mathrm{CIRA}}(z))\ \exp\left(-\frac{(z - z_0)^2}{\Delta z^2}\right) + n_{\mathrm{CIRA}}(z), \qquad z > z_0, \tag{A21}$$

where z_0 is the highest level of the NCEP model for a given latitude and longitude, $\Delta z = 5$ km. A formula similar to (A21) is used for the gradient ∇n.

A4. Calculating Geometrical Heights From Geopotential Height

The geometrical height or altitude (z) of an element P is defined as the distance of this element P to the reference mean sea level ellipsoid. The geopotential height of that element can be considered to be its geometric height plus (or minus) a correction, which depends upon latitude and height in a way that allows the dynamical equations to be applied more simply, without having to make additional adjustments for varying values of the gravitational acceleration and centrifugal force due to the Earth's rotation about its axis, and enables a single standard value of gravitational acceleration to be used along with geopotential height.

Geopotential Φ is related to altitude z [*List*, 1984],

$$\Phi = \int_0^h g(z, \varphi, \lambda)\, dz, \tag{A22}$$

where g is gravity acceleration at a given altitude z and latitude φ:

$$g = \frac{g_{re} R^2}{(R + z)^2}, \tag{A23}$$

where g_{re} is gravity acceleration on the reference ellipsoid at a given latitude; R is radius of the reference ellipsoid at that latitude. Performing integration in (A22) by using (A23) we obtain

$$\Phi = \frac{g_{re} R z}{R + z} \qquad \text{or} \qquad z = \frac{R\Phi}{g_{re} R - \Phi}. \tag{A24}$$

According to *Lambeck* [1988] we have

$$g_{re} = g_e\left(1 + f_2 \sin^2 \varphi - \frac{1}{4} f_4 \sin^2 2\varphi\right),$$

$$f_2 = -f \frac{5}{2} m - \frac{17}{14} fm + \frac{15}{4} m^2,$$

$$f_4 = -\frac{1}{2} f^2 + \frac{5}{2} fm,$$

where g_e is gravity acceleration at the equator of the reference ellipsoid, $g_e = 9.78032$ ms^{-1}, $f^{-1} = 298.275$, and $m = 0.00345$.

The difference between geometric and geopotential height is zero at the surface and increases with height. The difference varies with latitude. At 30° latitude the differences between geopotential and geometric height are ~0.3, 1.0, and 2.3 km at 40, 80, and 120 km altitudes, respectively.

Acknowledgments. We are grateful to R. Ware, M. Exner, R. Serafin, and R. Gall for their persistent support for the GPS/MET research. We also thank S. Mango from NOAA, whose support made it possible to complete this work. This work was supported by the Integrated Program Office of NOAA National Polar-orbiting Operational Environmental Satellite System under SMC/CIPN project Q000C1737600086 in support of the GPSOS/GPS team for NPOESS and by the National Science Foundation and the Federal Aviation Administration through a corporate agreement with NCAR and UCAR, ATM9209181, under scientific program EAR9405501.

References

Bean, B. R., and E. J. Dutton, *Radio Meteorology*, 435 pp., Dover, Mineola, New York. 1968.

Courtier, P., E. Andersson, W. Heckley, J. Pailleux, D. Vasiljević, M. Hamrud, A. Hollingsworth, F. Rabier, and M. Fisher, The ECMWF implementation of three-dimensional variational assimilation (3D-Var), I, Formulation, *Q. J. R. Meteorol. Soc*., *124*, 1783–1808, 1998.

Fjeldbo, G., G. A. Kliore, and V. R. Eshleman, The neutral atmosphere of Venus as studied with the Mariner V radio occultation experiments, *Astron. J*., *76*, 123–140, 1971.

Gorbunov, M. E., and A. S. Gurvich, MicroLab-1 experiment: Multipath effects in the lower troposphere, *J. Geophys. Res*., *103*, 13,819–13,826, 1998.

Gorbunov, M. E., and S. V. Sokolovskiy, Remote sensing of refractivity from space for global observations of atmospheric parameters, *Tech. Rep. 119*, Max Planck Inst. for Meteorol., Hamburg, Germany, 1993.

Gorbunov, M. E., A. S. Gurvich, and L. Bengtsson, Advanced algorithms of inversion of GPS/MET satellite data and their application to reconstruction of temperature and humidity, *Tech. Rep. 211*, 40 pp., Max Planck Inst. for Meteorol., Hamburg, 1996.

Kravtsov, Y. A., and Y. I. Orlov, *Geometrical Optics of Inhomogeneous Media*, 312 pp., Springer-Verlag, New York, 1990.

Kuo, Y.-H., X. Zou, S.-J. Chen, W. Huang, Y.-R. Guo, R. Anthes, D. Hunt, M. Exner, C. Rocken, and S. Sokolovskiy, A GPS/MET sounding through an intense upper-level front, *Bull. Am. Meteorol. Soc*., *79*, 617–626, 1998.

Kursinski, E. R., G. A. Hajj, K. R. Hardy, L. J. Romans, and J. T. Schofield, Observing tropospheric water vapor by radio occultation using the Global Positioning System, *J. Geophys. Res. Lett*., *22*, 2365–2368, 1995.

Kursinski, E. R., et al., Initial results of radio occultation observations of Earth's atmosphere using the global positioning system, *Science*, *271*, 1107–1110, 1996.

Kursinski, E. R., G. A. Hajj, J. T. Schofield, R. P. Linfield, and K. R. Hardy, Observing Earth's atmosphere with radio occultation measurements using the Global Positioning System, *J. Geophys. Res*., *102*, 23,429–23,465, 1997.

Lambeck, K., *Geophysical Geodesy*, 718 pp., Oxford Univ. Press, New York, 1988.

Leroy, S. S., The measurement of geopotential heights by GPS radio occultation, *J. Geophys. Res*., *102*, 6971–6986, 1997.

List, R. J., Smithsonian meteorological tables, *Smithson. Misc. Collect*., *114*, 217–490, 1984.

Peaceman, D. W., and H. H., Rachford, The numerical solution of parabolic and elliptic differential equations, *J. Soc. Ind. Appl. Math*., *3*, 28–41, 1955.

Press, W. H., B. P. Flannery, S. A. Teukolsky, and W. T. Vetterling, *Numerical Recipes*, 702 pp., Cambridge University Press, New York, 1992.

Rees, D., J. J. Barnett, and K. Labitzke, COSPAR International Reference Atmosphere, II, Middle atmosphere models, *Adv. Space Res*., *10*(12), 517 pp., 1990.

Rocken, C., et al., Analysis and validation of GPS/MET data in the neutral atmosphere, *J. Geophys. Res*., *102*, 29,849–29,866, 1997.

Runcorn, S. K., *International Dictionary of Geophysics*, Pergamon, vol. 1, 584 pp., New York, 1967.

Sela, J. G., Spectral modeling at the National Meteorological Center, *Mon. Weather Rev*., *108*, 1279–1292, 1980.

Vorob'yev V. V., and T. G. Krasilnikova, Estimation of the accuracy of the atmospheric refractive index recovery from Doppler shift measurements at frequencies used in the NAVSTAR system, *Phys. Atmos. Ocean*, *29*, 602–609, 1994.

Ware, R., et al., GPS sounding of the atmosphere from low earth orbit: Preliminary results, *Bull. Am. Meteorol. Soc*., *77*, 19–40, 1996.

Yanenko, N. N., *The Method of Fractional Steps*, translated by M. Holt, Springer-Verlag, New York, 1971.

Zou, X., Y.-H. Kuo, and Y.-R. Guo, Assimilation of atmospheric radio refractivity using a nonhydrostatic adjoint model, *Mon. Weather Rev*., *123*, 2229–2249, 1995.

Zou, X., F. Vandenberghe, M. Pondeca, and Y.-H. Kuo, Introduction to adjoint techniques and the MM5 adjoint modeling system, *NCAR Tech. Note*, *NCAR/TN-435-STR*, Natl. Cent. for Atmos. Res., 1997.

R. A. Anthes, University Corporation for Atmospheric Research, Boulder, CO 80303.

J. C. Chang, Central Weather Bureau, Taipei, Taiwan.

M. E. Gorbunov and S. Sokolovskiy, Institute of Atmospheric Physics, Moscow, Russia.

Y.-H. Kuo and F. Vandenberghe, National Center for Atmospheric Research, Boulder, CO 80307.

J. G. Sela, National Centers for Environmental Prediction, Camp Springs, MD 20233.

B. Wang, LASG, Institute of Atmospheric physics, CAS, Beijing, P. R. China.

X. Zou, Dep. of Meteorology, Florida State University, 404 Love Bldg., Tallahassee, FL 32306. (zou@met.fsu.edu)

(Received April 7, 1999; revised June 3, 1999;
accepted June 14, 1999.)